Coastal Engineering 64 (2012) 1–15

Contents lists available at SciVerse ScienceDirect

Coastal Engineering

journal homepage: www.elsevier.com/locate/coastaleng

Turbulent flow structure in experimental laboratory wind-generated gravity waves

Sandro Longo [a,*], Dongfang Liang [b], Luca Chiapponi [a], Laura Aguilera Jiménez [c]

[a] Department of Civil Engineering, University of Parma, Parco Area delle Scienze, 181/A, 43100 Parma, Italy
[b] Department of Engineering, Trumpington Street, Cambridge CB2 1PZ, UK
[c] Instituto Interuniversitario de Investigación del Sistema Tierra, Universidad de Granada, Avda. del Mediterráneo s/n, 18006 Granada, Spain

ARTICLE INFO

Article history:
Received 1 December 2011
Received in revised form 7 February 2012
Accepted 8 February 2012
Available online xxxx

Keywords:
Free surface turbulence
Wind-generated waves
Laboratory experiments

ABSTRACT

This paper is the third part of a report on systematic measurements and analyses of wind-generated water waves in a laboratory environment. The results of the measurements of the turbulent flow on the water side are presented here, the details of which include the turbulence structure, the correlation functions, and the length and velocity scales. It shows that the mean turbulent velocity profiles are logarithmic, and the flows are hydraulically rough. The friction velocity in the water boundary layer is an order of magnitude smaller than that in the wind boundary layer. The level of turbulence is enhanced immediately beneath the water surface due to micro-breaking, which reflects that the Reynolds shear stress is of the order u_w^2. The vertical velocities of the turbulence are related to the relevant velocity scale at the still-water level. The autocorrelation function in the vertical direction shows features of typical anisotropic turbulence comprising a large range of wavelengths. The ratio between the microscale and macroscale can be expressed as $\lambda/\Lambda = a\,\mathrm{Re}_\Lambda^n$, with the exponent n slightly different from $-1/2$, which is the value when turbulence production and dissipation are in balance. On the basis of the wavelength and turbulent velocity, the free-surface flows in the present experiments fall into the wavy free-surface flow regime. The integral turbulent scale on the water side alone underestimates the degree of disturbance at the free surface.

1. Introduction

Interaction and material exchange at the gas–liquid interfaces occur in geophysical flows, industrial processes and biological systems. The scales of these processes vary significantly, leading to the change in the relative importance of the different contributing mechanisms. The two boundary layers, one above and the other beneath the interface, are coupled by a thin water layer in the order of a tenth of millimetre, which appears to control most of the transfer process. A tiny quantity of surfactant can dramatically modify the gas-transfer behaviour without interfering with the fluid velocity and turbulence (McKenna, 2000). Different types of surfactant are present in industrial processes as catalysts for chemical reactions, and are also naturally present in seas, lakes and wherever biological organisms are present. Early models of transfer at the interface were based only on the thin-film assumption, and were soon improved by the models based on the diffusion assumption, such as the 'penetration' model (Higbie, 1935). Later, a surface renewal mechanism, controlled by turbulence, was proposed as the most important contributor to transfer processes (Dankwerts, 1951). All of these conceptual models rely on experiments performed to evaluate empirical coefficients, which are related to the characteristics of the flow field. A theoretical analysis on near-wall turbulent exchange (Sirkar and Hanratty, 1970) was based on a slip-free interface assumption in a co-current air–water flow by McCready et al. (1986). These authors related the transfer coefficients at the interface to the spectrum of the gradient of vertical velocity fluctuations. Following the similar idea, Tamburrino and Gulliver (2002) analysed the moving-bed flume results to evaluate the transfer coefficients.

The interface is subject to turbulence effects on both the gas (air) side and the liquid (water) side, but the resistance to the mass, heat, chemical and momentum transfer mainly comes from the liquid side. Hence, special attention is paid to the aqueous boundary layer. If the only effect of turbulence is to deform the interface, then it would increase the contact area and, hence, enhance the fluxes. Several shapes of free-surface deformation can be observed in nature, but, by far, the most typical one is waves, ranging from capillary waves of a few micrometers long to tsunamis with wavelengths of hundreds of kilometres. Gravity waves are often accompanied by currents. In particular, a drift layer close to the free surface is ubiquitous in wind-generated waves. Because this drift layer is so close to the interface, it plays a preeminent role in the mixing and transfer of physical quantities. Field studies (Bye, 1965; Churchill and Csanady, 1983) and laboratory studies (Shemdin, 1972; Wu, 1975) revealed that the water velocity profiles in the drift layer are logarithmic. Cheung and Street (1988) showed that, at wind speeds greater than 3.2 m s^{-1}, the flow in the water boundary layer is hydrodynamically rough, while Wu (1975) demonstrated it to be either hydrodynamically

* Corresponding author. Tel.: +39 0521 90 5924; fax: +39 0521 90 5157.
E-mail address: sandro.longo@unipr.it (S. Longo).

0378-3839/$ – see front matter © 2012 Elsevier B.V. All rights reserved.
doi:10.1016/j.coastaleng.2012.02.006

smooth or in the transition stage (Bye, 1965). In some tests, the experimental value of the von Karman constant was found to exceed 0.4 (Cheung and Street, 1988), suggesting the hydrodynamic process to be more complex than that involved in the conventional flat plate boundary layer.

The behaviour of turbulent boundary layers depends on the level of deformation of the interface. All of the experimental studies of the interfacial processes in the presence of turbulence contains the specific turbulence generation mechanism, such as two-dimensional (2D) open channels (e.g., Komori et al., 1989), moving-bed flumes (Tamburrino and Gulliver, 1999), grid-stirred tanks (e.g., Brumley and Jirka, 1983), towed hydrofoils submerged near the free surface of a flow channel (Battjes and Sakai, 1981) and spilling-type breakers generated on a steady current by a Crump weir (Longo, 2010, 2011). Early investigations studied non-wavy slip interfaces with the turbulence generated by wind or water shear (Lam and Banerjee, 1992; Rashidi and Banerjee, 1990). Other studies examined turbulence structure and mass transfer of wavy gas–liquid interfaces, where the wind action serves as the source of turbulence and is also responsible for the generation of the gravity waves (Komori et al., 1993). The coherent structures of turbulence are of great importance, as they are efficient in generating convective flows and are responsible for enhancing the transfer processes. The three-dimensional (3D) structure of turbulence has been studied close to a Crump weir in a flume (Longo, 2010, 2011) obtaining indications about the shapes of the coherent structures impinging the interface from the water side. In addition, these coherent structures have been correlated with the free-surface deformation.

A better description of the air–water boundary conditions is also essential in order to improve the accuracy of numerical models (see e.g. Brocchini and Peregrine, 2001a,b and Brocchini, 2002).

In the present study, the flow field is generated by wind blowing over a water tank. The velocity and water level are measured using an ultrasound velocity profiler (UVP), and the velocity is also measured by a Laser Doppler Velocimetry (LDV). A series of experiments have been completed, and numerous results concerning the air-side boundary layer and the free-surface statistics have already been analysed and reported in other papers (Longo, 2012). These earlier papers are referenced whenever the characteristics of the overall flow phenomena are required in the description herein.

As a common limitation for most of the previous experimental investigations (Lam and Banerjee, 1992; Rashidi and Banerjee, 1990), the present experimental setup is only two-dimensional, so some dynamic mechanisms of turbulence, e.g. vortex stretching, cannot be directly evaluated. Due to the restriction of the laboratory conditions, a three-dimensional investigation has not been possible. Care has been taken in interpolating the results, and all the instruments used have been validated against other independent experiments and analytical solutions.

This paper is organised as follows. In Section 2, the experimental apparatus and the measurement techniques are briefly described. Section 3 analyses the mean velocity and the turbulence structure in the water-side boundary layer, while Section 4 is devoted to the spatial structure of the turbulence and the length scales. The conclusions are presented in the last section.

2. Experimental apparatus

The experiments were conducted in a small non-closed low-speed wind tunnel at the Centro Andaluz de Medio Ambiente, CEAMA, University of Granada, Spain. The boundary layer wind tunnel is composed of poly(methyl methyl acrylate) (PMMA) with a test section of 3.00 m in length and a cross-section of 360 mm × 430 mm. A water tank was installed for gravity wave generation. The water tank is constructed of PVC with a length of 970 mm and a height of 395 mm (internal size). The still-water depth is fixed at 105 mm. One side of the tank is made of 5 mm thick glass with good transparency to allow LDV measurements. Numerous measures have been adopted to optimally control the mean water level in the tank during the experiments so as to avoid wave reflection and overtopping. A layout of the apparatus is shown in Fig. 1, the details of which can be found in Chiapponi et al. (2011) and Longo (2012).

2.1. The Laser Doppler Velocimetry (LDV)

The water flow measurement is carried out with a TSI 2D Laser Doppler Velocimetry (LDV) system. The laser source is an Innova 70 Series water-cooled Ar ion laser, which reaches a maximum power of 5 W and emits two pairs of laser beams having different wavelengths, namely green ($\lambda_g = 514.5$ nm) and blue ($\lambda_b = 488.0$ nm). The TSI optical modular system has a two-component fibre-optic transmitting/receiving probe, which also collects the backward-scattered light and sends it to the processing unit. The measurement volume is defined by the intersection of the four laser beams, and takes the shape of a prolate ellipsoid with the dimensions of about 0.08 mm × 0.08 mm × 1.25 mm. The transmitting/receiving probe of the LDV is mounted on an ISEL traverse system and placed adjacent to the wind tunnel (Fig. 2). The traverse system allows the displacement of the probe in both horizontal (parallel to the wind tunnel) and vertical directions, with an estimated positional accuracy of 0.1 mm. Instructions for the traverse system are written in a MATLAB® programme that transfers data to an ISEL C142 4.1 controller.

As indicated in Fig. 1, the coordinate system for the transverse displacements has its horizontal origin ($x = 0$) on the left of the tank with the positive direction pointing toward the fan, and its vertical origin ($z = 0$) at the still-water level with the positive direction pointing upward. A negative inclination of the probe with an angle $\beta = -6.5°$ enables the velocity measurement to be very close to the free surface. When water is still, the system could measure the Brownian movement of the particles in the skin layer, which has been used to determine the origin of the vertical coordinate with an accuracy in the order of the vertical size of the measurement volume, $\approx 1/10$ mm. When waves are present, some measurements can be conducted above the still wave level, i.e. in the wave crests. In order to increase the accuracy of the measurement close to the interface, the laser reference frame has been rotated by an angle $\theta = 45°$ with respect to the coordinate system (x, z). Very clear water was used in the experiments, which is seeded with suitable particles to enhance the quality of the measurements. After several trials, TiO_2 particles, usually adopted as tracers for Ultrasound measurements and with size of a few micrometers, were selected as an appropriate tracer. The strong effects of the surfactants on water wave generation require the free surface to be cleaned regularly. At the beginning of each day of testing, water in the tank is replaced with fresh clean water, and the seeding particles are gradually added until the correct tracer concentration in the water is reached.

2.2. The ultrasonic Doppler velocity profiler (UVP)

Measurements of the fluid velocity beneath the free surface are conducted with a single vertical probe connected to an ultrasonic Doppler velocity profiler (Model DOP2000, 2005; Signal Processing, Switzerland) with a probe carrier frequency of 8 MHz (Model TR0805SS). The active element of the transducer has a diameter of 5 mm housed in an 8-mm-diameter metal cylinder. The probe is 30 mm in length, and the origin of the measurements is 38 mm above the bottom of the tank, i.e., 67 mm below the still-water level (Fig. 1). By seeding water with TiO_2 particles, as used for the LDV measurements, the signal to noise (S/N) ratio in the UVP measurement is also increased. The transducer measures the axial velocity components at 100 positions, starting from 3 mm in front of the

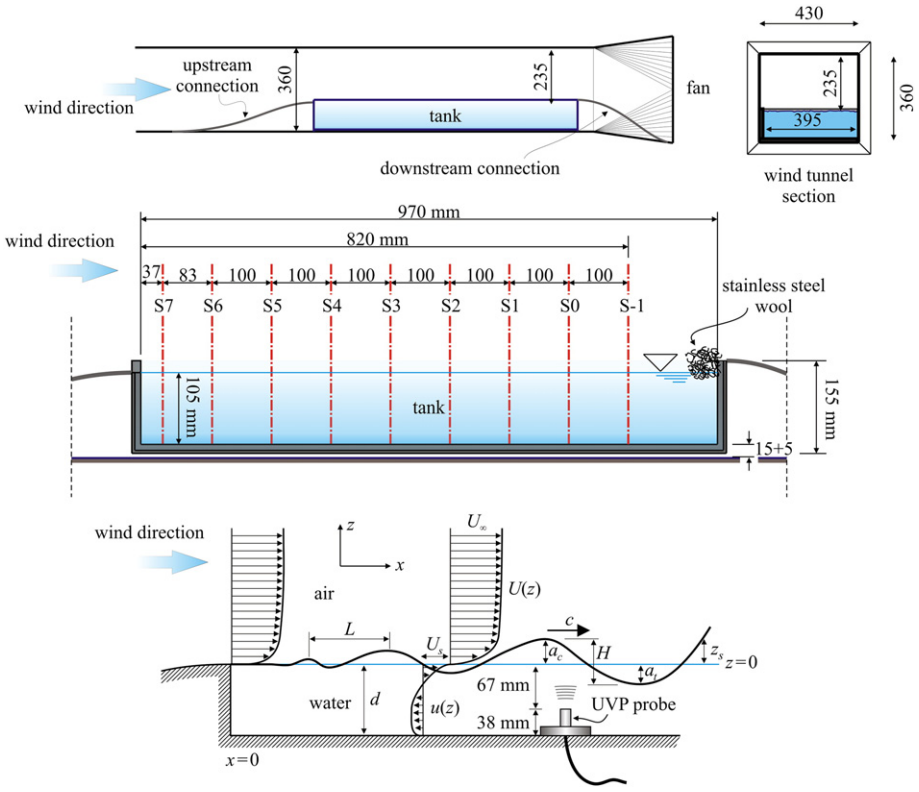

Fig. 1. Layouts of the wind tunnel and the water tanks.

probe head and with an interval of 0.75 mm. The measurement volume at each position is shaped as a disk, whose thickness is related to the operating condition and whose diameter is equal to 5 mm in the near field zone (the near field zone extension is around 33 mm far from the probe). The size of the measurement volume increases in the far field zone because of the lateral spreading of the ultrasonic (US) energy, with a diverging half angle of 1.2°. The thickness of the sampling volumes can be assumed to be equal to half of the wavelength contained in a burst unless the electronic bandwidth of the instrument is limited. In the present experimental setup, the minimum thickness of the sampling volume is 0.68 mm.

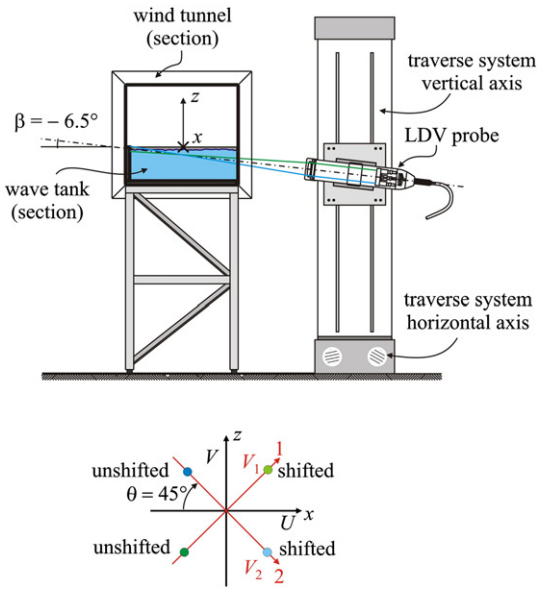

Fig. 2. The layouts of the LDV probe and the reference systems.

The overall size of the measurement volumes only allows the detection and analysis of macro-turbulence, but this limitation is outweighed by some advantages. For example, a large number of measurement points are almost simultaneously available. The measurements at consecutive positions are not concurrent, and the time lag of the pulse from one position to the next is $k\delta z/c$, where k is a coefficient (~2), δz is the distance between two nearby positions and c is the ultrasound celerity in water. The largest dimension of the measurement volume is in the horizontal direction. For the flow field of the present experiments, the fluid velocity only has a moderate spatial gradient in the horizontal direction. The largest spatial gradient is in the vertical direction. The current UVP setup attains a vertical resolution that is comparable to the resolution obtained using LDV, particle image velocimetry (PIV) or thermal anemometry. The velocity resolution along the probe axis is 1/128 (1 least significant bit) of the velocity range (~0.8% FS). For all of the tests, this resolution is finer than 4 mm/s. The overall accuracy of the velocity measurements under carefully controlled conditions has been assessed to be 3% of the instantaneous value (Longo, 2010).

2.3. Calibration of the UVP

Calibration of the UVP was performed by comparing the mean velocity and turbulence level measurements with those obtained by the PIV. The calibration in terms of turbulence estimation is very important, because certain parameters do not influence the estimation of the mean value but affect the estimation of turbulence. This problem is common in velocity-measuring instruments: in LDV, the bandwidth of the filters in the signal processor only affects the intensity of the recorded fluctuations.

The calibration is performed by taking measurements in a flume for two different conditions: (a) with and (b) without a hydrofoil used to increase the turbulence level without changing the mean velocity. A TSI PIV is used with a data rate of 3.75 frames/s, a time step of 2000 μs between the coupled frames and a spatial resolution of

0.11 mm/pixel in the adopted configuration. The interrogation window is 32×32 pixels with 50% overlap. Hence, the velocity vectors are given in a 1.8-mm-spaced grid, which is comparable to the interval between two nearby position in the UVP measurement. The acquisition lasts for 700 frames in the case without the hydrofoil and for 100 frames in the case with the hydrofoil. The setup of the UVP acquires 40,000 profiles at a data collection rate of about 200 Hz for 100 positions spaced 0.75 mm apart. During the post-processing, the ultrasound celerity is corrected according to the water temperature, which is equal to 23.58±0.01 °C and 24.02±0.01 °C in the two tests respectively. The typical velocity profiles and the turbulence profiles are given in Fig. 3, which correspond to 16 emissions per profile with a burst length of 4 waves. The error bars for the UVP are 3% of the measured value (Longo, 2010), and the expected uncertainty for the PIV data can be assumed to be ±1% of the measured value (not shown in the diagrams). The velocity and turbulence profiles show good agreement in both tests, characterised by the levels of turbulence equal to 8% and 16% respectively. The PIV measurement of the velocity with the presence of a hydrofoil shows some fluctuations due to the reduced number of frames (100 frames, ~27 s).

2.4. Detecting the free-surface level with the UVP

The UVP signal can also be used to detect the instantaneous free surface level. In fact, the echo of the emitted ultrasound packets, once reflected by the water surface, shows a large increase in energy (the signal is saturated for most of the time). Hence, a detecting algorithm can be designed to estimate the instantaneous position of the free surface. The detecting algorithm locates the point nearest to the free surface where saturation occurs or the position where the maximum echo is recorded. In the present setup with 100 positions spaced 0.75 mm apart in each profile, the last measurement volume is 75 mm away from the probe. The typical mean water level is 65 mm away from the probe in the experiment, therefore the maximum recordable crest level 10 mm. A total of 60,000 profiles were recorded in each test, with a data collection rate equal to about 100 profiles per second. The instantaneous water level is measured with a resolution equal to the distance between two subsequent positions (0.75 mm in the present setup). Occasionally, a spike occurred, and it is filtered out by applying the algorithm developed by Mori et al. (2007). The accuracy and reliability of the measurements have been checked by comparing with the measurements of the resistance probes (Chiapponi et al., 2011), which reveals excellent agreement. In analysing the water velocity data, the information on the free-surface level is very useful in determining the last valid point in the velocity profile.

3. Mean velocity, Reynolds stresses and turbulence

3.1. Separating turbulence flow

The instantaneous velocity field is usually decomposed into three components:

$$U(z,t) = \bar{U} + \tilde{U}(z,t) + U'(z,t) \tag{1}$$

where $\bar{U}$ is the mean velocity, $\tilde{U}$ is the wave-induced component and U' is the turbulent component. The mean velocity coincides with the ensemble velocity if the ergodic hypothesis holds. We can also define a space average of U:

$$\langle U \rangle = \int_V U(\mathbf{x}+\mathbf{s},t)a(\mathbf{s})dV, \tag{2}$$

where $\mathbf{s}$ is a space vector describing the volume of integration V and $a(\mathbf{s})$ is a weighting function. Introducing a phasic function, which is $X_j(\mathbf{x},t)=1$, if the vector position $\mathbf{x}$ is in the phase j at the time t, and is $X_j(\mathbf{x},t)=0$ otherwise. Then, we can define the phasic average as

$$\widehat{U} = \frac{\int_V X_j(\mathbf{s},t)U(\mathbf{x}+\mathbf{s},t)a(\mathbf{s})dV}{\int_V X_j(\mathbf{s},t)dV} = \frac{\left\langle X_j(\ldots)\right\rangle}{\left\langle X_j\right\rangle} = \frac{\left\langle X_j(\ldots)\right\rangle}{\Phi_j}, \tag{3}$$

where Φ_j is called the volume fraction, concentration or intermittency factor of the j phase. The phasic average and Reynolds average are equivalent in the domain where the phase j is always present; otherwise, the phasic average includes only the velocities that contain the phase j.

The average can be in an Eulerian frame or Lagrangian frame, with the origin at the instantaneous free-surface level.

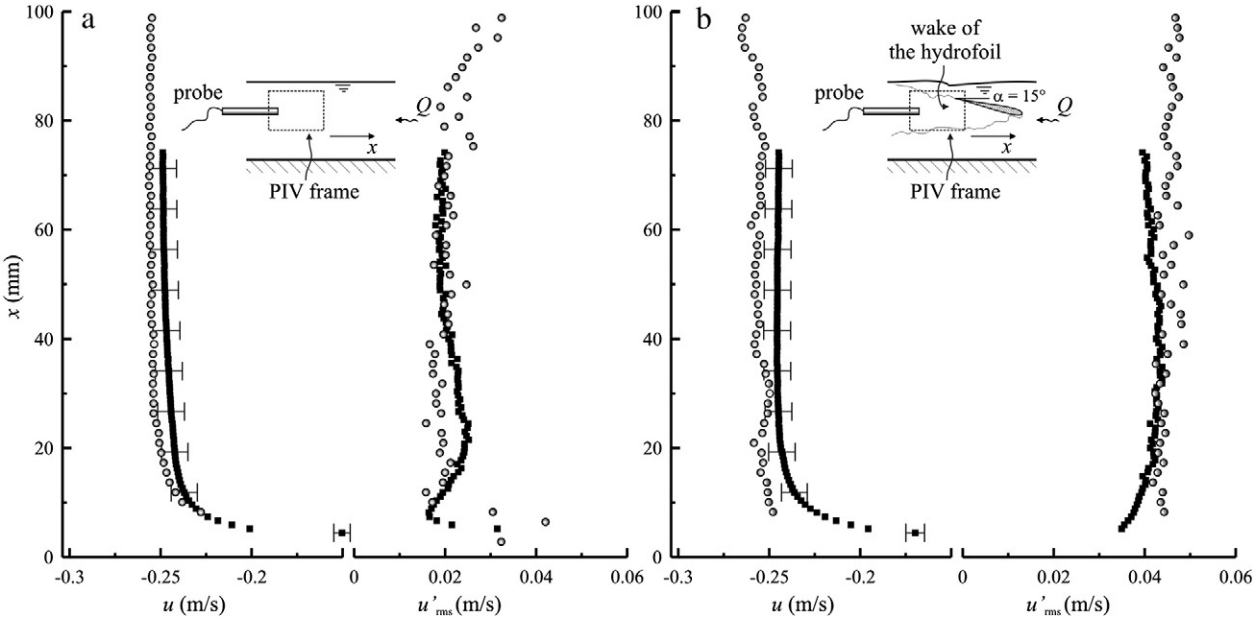

Fig. 3. The calibration of the UVP vs. the PIV. a) Velocity and turbulence in a flume. b) Velocity and turbulence in a flume with a wake generated by a hydrofoil. ■ UVP data; ◍ PIV data.

The problem of separating the waves and eddies remains unresolved, and well-tested methods only exist in some specific situations. None of the previously proposed techniques (Dean, 1965; Nadaoka, 1986; Siddiqui and Loewen, 2007; Thais and Magnaudet, 1996; Thornton, 1979) are rigorously applicable to the present conditions, because the waves experience micro-breaking and their shape is strongly influenced by wind. In this study, the separation of the different contributions is achieved by using the filtering method, assuming that, below a frequency threshold, the velocity is due to waves and all of the residual contributions are due to turbulence. The cut-off frequency for the velocity time series was chosen by observing the power spectrum of the velocity (horizontal and vertical). As will be seen later, the power spectrum generally shows a strong peak at around 5 Hz, with an almost linear decay at higher frequencies. The threshold frequency has to be based on subjective judgment, and a certain degree of arbitrariness is involved in the choice of the cut-off frequency. The present experiments simply assume $f_{co} = 10$ Hz for all of tests.

3.2. Measurements with LDV

3.2.1. The mean flow and the friction coefficient

The first set of measurements was conducted by using the LDV in four different sections. The data collection rate is greater than 1 kHz. The mean velocity profiles are shown in Fig. 4. The inset shows a schematic diagram, with the tangential stress acting on the free surface and the forward and return drift currents on the two ends of the water tank.

The wind blowing from the left to the right sets up the surface displacement, together with the forward and return drift currents. A vertical positive velocity component is expected at small fetches, and a vertical negative velocity component is expected at larger fetches. The main characteristics of the flow field are drawn in Fig. 5, where the sub-surface boundary layer and the bottom boundary layer are sketched. There is a surface of zero horizontal velocity, which separates the positive drift current and the undertow current. We do not have direct measurements near the bottom of the tank but a rough estimation of the expected geometry is possible. The bottom boundary layer, based on the Reynolds number defined as $\mathrm{Re}_x = u_\infty x/\nu$, with $u_\infty \approx 0.05$ m/s, should not be turbulent, since the maximum value is only $\mathrm{Re}_x \approx 4\times10^4$. However, it is not a classical boundary layer over a flat plate with little incoming turbulence. The external stream, with respect to the bottom boundary layer, has a turbulence index greater than one. Also a circulation in the boundary layer is set up consisting of the vertical velocity component. A rough estimation of the thickness of the bottom boundary layer at $x = 0.85$ m, in Section S6 is $\delta \approx 5\sqrt{\nu x/u_\infty} = 4$ mm. It is a small fraction of the local depth, so the bottom boundary layer has a very limited effect on this current. The following considerations are required for a proper mass balance analysis. First of all, the maximum horizontal velocity at the free surface is in a domain where the water concentration is less than one, giving a positive flux smaller than that apparent in the velocity plots. Second, there is a three dimensional flux: near the lateral wall of the water tank the wind stream action is limited by the wall boundary layer. As a consequence, the positive drift current there is smaller than that along the centreline of the tank, allowing a stronger return current near the lateral wall.

The typical drift current near the surface has greater strength at larger fetches. Some data are above the still-water level due to the wind and wave setup, and the occasional measurement taken in the wave crests. It is difficult to directly estimate the surface drift from the horizontal velocity profiles due to the strong gradient. The present data give the Eulerian surface drift, usually considered as the superposition of the wind-induced drift (Wu, 1975) and the Stokes drift:

$$U_s = U_{sw} + U_{sS} \tag{4}$$

In order to compare the present experimental data with previous data and theoretical analysis we analyse separately the effects of the two contributions. The wind-induced drift is related to the friction velocity of the air flow u_{*a} and is assumed to be equal to (Wu, 1975)

$$U_{sw} = 0.53 \cdot u_{*a} \tag{5}$$

As seen in the results of the air flow boundary layer profiles in Table 1, the values for u_{*a} is in the range 0.4–0.7 m/s. Hence, a wind-induced drift in the range 0.21–0.39 m/s is expected. The rough evaluation of the profiles shown in Fig. 4 gives lower values, with a proportionality coefficient between U_{sw} and u_{*a} equal to ~0.4. Indeed, the original derivation of Eq. (5) is based on experiments with wind speed between 3 m/s and 14 m/s, and the measured ratio U_{sw}/u_{*a} shows a large scatter in the range 0.4–0.7. The lower values refer to wind speed larger than 10 m/s (see Fig. 6 in Wu, 1975) hence the present experiments give results in accordance to those reported in Wu (1975).

The Stokes contribution U_{sS} can be estimated as

$$U_{sS} = c_0 \left(\frac{\pi H}{L}\right)^2, \tag{6}$$

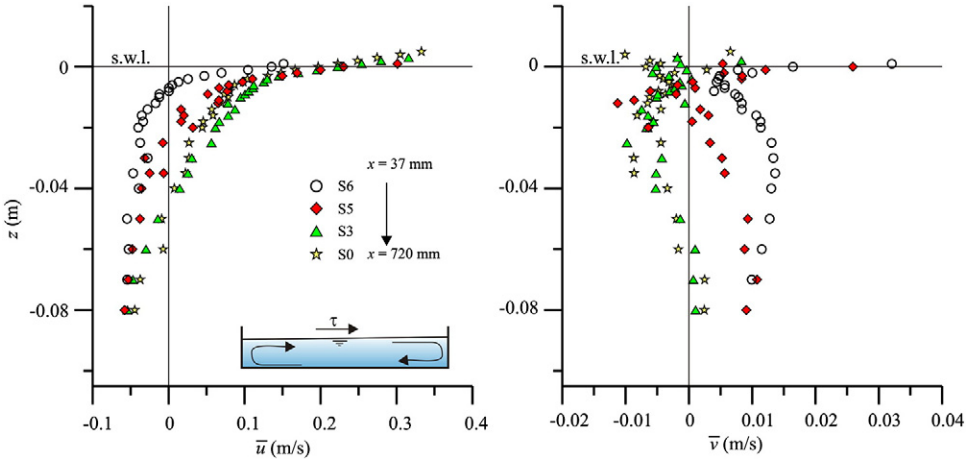

Fig. 4. The horizontal and vertical mean water velocity profiles. The asymptotic wind speed in the free stream is $U_\infty = 10.74$ m/s. The inset shows the schematic diagram of the current in a closed tank with the tangential stress acting on the free surface.

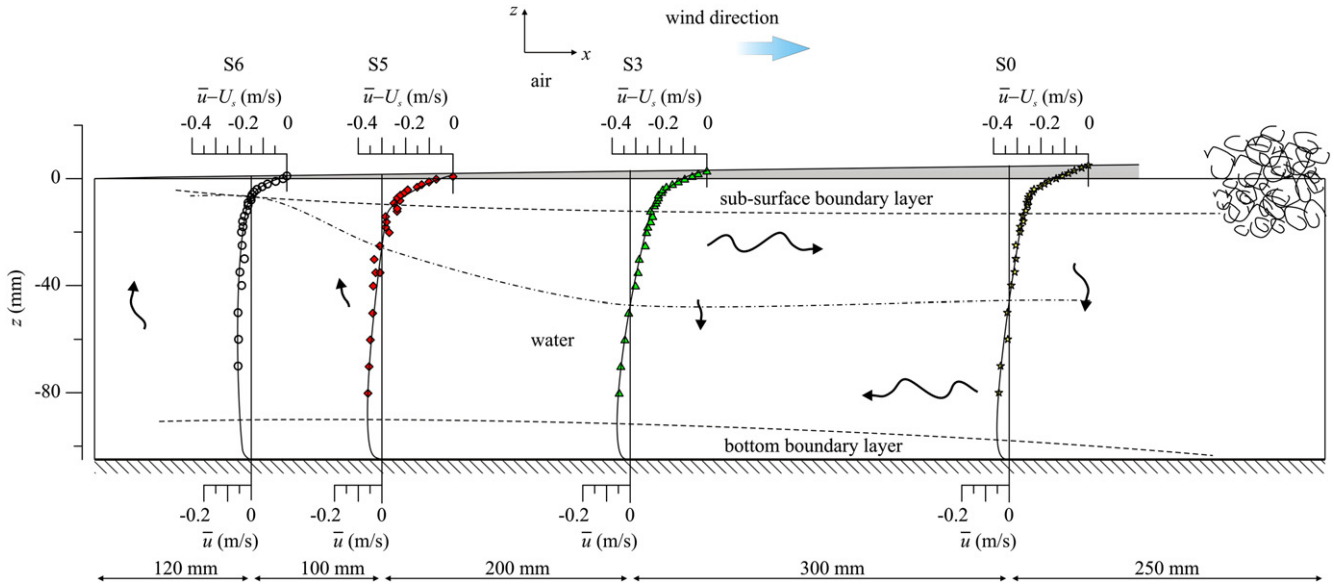

Fig. 5. Synoptic view of the horizontal velocity profiles. The dashdot curve is the trace of the surface of zero horizontal velocity which defines the limit between the drift positive current and the undertow current.

where c_0 is the phase celerity in absence of current, H is the wave height and L is the wavelength. Eq. (6) is based on the first order solution. For non-linear waves, either in the surf zone or for steep waves eventually breaking at high wind velocities, a different expression is expected. Svendsen (1984) shows the detailed calculation of mass flow in a generic wave flow field, and Williams (1981) shows the detailed Stokes drift computation with nonlinear and periodic water waves. A rough estimate of the Stokes drift in Section S0 shows that the measured wave has a height of 5.64 mm, a length of 120 mm and a phase celerity of 0.37 m/s. The Stokes drift computed according to Eq. (6) is equal to 8 mm/s, which turns out to be only a few percent of the total drift.

The mean water velocity profile with respect to the moving water surface follows a linear relationship, rather than a logarithmic profile, near the free surface at depths less than three times the root mean square wave amplitude. In the logarithmic profile region, the general fitting curve is

$$\frac{\bar{u}-U_s}{u_{*w}} = \frac{1}{k}\ln\frac{z}{k_s} + 8.5, \tag{7}$$

where u_{*w} is the friction velocity, k is the von Karman constant and k_s is the roughness length. Eq. (7) can also be written as

$$u^+ = \frac{1}{k}\ln z^+ + C, \tag{8}$$

where $u^+ = (\bar{u}-U_s)/u_{*w}$, $z^+ = zu_{*w}/\nu$. The constant C is equal to

$$C = 8.5 - \frac{1}{k}\ln k_s^+, \tag{9}$$

where $k_s^+ = k_s u_{*w}/\nu$. In Section S6, the flow is hydrodynamically smooth, so the fitting curve can be simplified as:

$$\frac{\bar{u}-U_s}{u_{*w}} = \frac{1}{k}\ln\frac{zu_{*w}}{\nu} + 5.5. \tag{10}$$

The curve fitting gives a correlation coefficient always greater than 0.92. The values of the coefficients are presented in Table 2 and the normalised profiles of the time-averaged streamwise velocity in wall coordinates at different fetches are presented in Fig. 6. Also plotted for reference are the universal law of the wall for turbulent flows with zero pressure gradient in smooth flow and at the beginning of the fully turbulent regime (Schlichting and Gersten, 2000, pp. 526–532). For comparison, the data from Cheung and Street (1988) and the semiempirical model results by Kudryavtsev et al. (2008) are also shown. The experimental data refer to wind speed ranging from 1.5 m/s to 13.1 m/s. Cheung and Street note that the different slope of the intermediate wind velocity can be attributed to the wave dynamics effects, as it cannot be a consequence of the pressure gradients, the choice of the origin of the z^+ coordinate, the possible three dimensionality of the flow, or the shift in the measured velocity due to the mean flow following the water surface. The curves show the model prediction for two of the Cheung and Street experiments.

Table 1
The parameters for the mean air flow velocity profiles at different fetches. The measurements are in air over water. x is the fetch length, U_∞ is the wind asymptotic velocity, u_{*a} is the friction velocity of the air stream.

Section #	S6	S5	S3	S0
x (mm)	120	220	420	720
U_∞ (m/s)	10.50	10.93	10.74	10.92
u_{*a} (m/s)	0.40	0.74	0.68	0.63

Table 2
The parameters for the mean water flow velocity profiles at different fetches. The measurements are in water. x is the fetch length, u_{*w} is the friction velocity of the water stream, k_s is the roughness length, C is the constant in the non dimensional velocity profile, Re_x is the Reynolds number based on x and on u_∞.

Section #	S6	S5	S3	S0
x (mm)	120	220	420	720
u_{*w} (m/s)	0.0095	0.0257	0.0318	0.0257
k_s (mm)	–	7.7	26.7	7.6
C	5.5	−5.57	−8.34	−4.68
Re_x ($\times 10^3$)	24	77	147	252

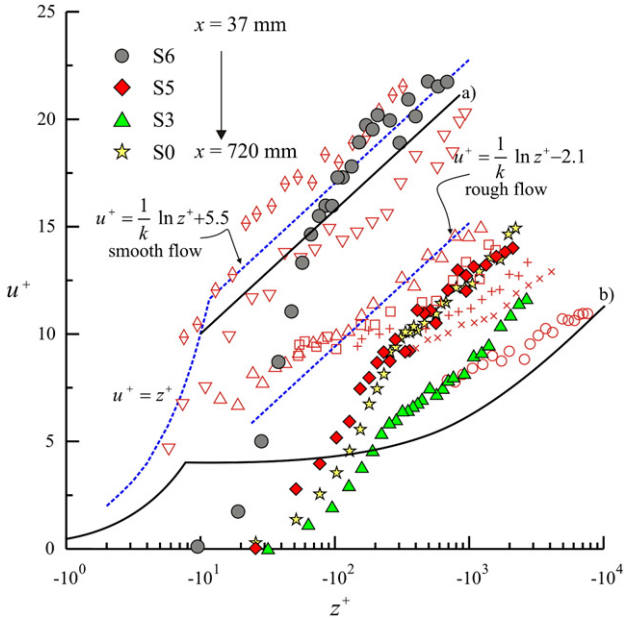

Fig. 6. The normalised profiles of the time-averaged streamwise velocity in wall coordinates at different fetches. Filled symbols: data from the present experiments. Empty symbols: data from Cheung and Street (1988). ◇ 1.5 m/s; ▽ 2.6 m/s; △ 3.2 m/s; □ 4.7 m/s; + 6.7 m/s; × 9.9 m/s; ○ 13.1 m/s. Continuous line: model by Kudryavtsev et al. (2008) fitted to Cheung and Street data: a) fitted to 2.6 m/s; b) fitted to 13.1 m/s. Also plotted for reference is the universal law of the wall for turbulent flows with zero pressure gradient in smooth flow and at the beginning of the fully turbulent regime.

According to the model, the deviation of the velocity profile from the universal law for smooth surface is due to direct injection of momentum and energy from small-scale breaking into the water body. It seems that a shift in the origin is responsible for an apparent extension of the viscous region in the present data with respect to the results by Cheung and Street and Kudryavtsev et al. (2008), even though the possible errors in detecting the origin cannot be solely responsible for all the shifts. In addition, the present experiments and the experiments by Cheung and Street are not exactly comparable, because both the shift velocity and the peak frequency of the waves are very different (≈2 Hz in Cheung and Street and ≈5 Hz in the last section for the present experiments).

The friction coefficient C_f is defined by

$$C_f = \frac{\tau}{\rho_w u_\infty^2} = \left(\frac{u_{*w}}{u_\infty}\right)^2, \tag{11}$$

where τ is the tangential stress and u_∞ is the free stream velocity. C_f is plotted against the Reynolds number $\mathrm{Re}_x = u_\infty x/\nu$ in Fig. 7. The free stream velocity is evaluated by observing the velocity profiles and is equal to 0.20 m/s for Section S6 and 0.35 m/s for the other sections. These values have been confirmed by fitting the measured velocities using Eq. (8), where different drift velocities have been inserted. Indeed, the free stream velocity is quite important for the correct evaluation of the friction coefficients. Wu (1975) adopted the drift velocity as the velocity scale, which is equal to the free stream velocity in very large tanks but is slightly modified in small tanks due to the return current. The adopted values for the present experiments The theoretical friction coefficient is equal to

$$\begin{cases} C_f = 0.332\cdot \mathrm{Re}_x^{-1/2} & \text{laminar flow} \\ C_f = 0.0295\cdot \mathrm{Re}_x^{-1/5} & \text{smooth turbulent flow} \\ 1.458\left(2C_f\right)^{-2/5} - \ln\sqrt{C_f} = \ln \mathrm{Re}_x & \text{fully turbulent rough flow} \end{cases}. \tag{12}$$

The last expression is computed using the empirical equation $C_f = 0.5[2.87 + 0.686\ln(x/k_s)]^{-5/2}$, where k_s is the geometric scale of the roughness and the fully turbulent rough flow is assumed to be reached at $k_s u_{*w}/\nu = 70$.

The surface drag coefficient of the wind-induced water flow generally follows the value of the fully-rough turbulent flow regime, except for the most upstream section, which follows the smooth turbulent flow regime. Notably, in Section S3, where the friction factor experiences a jump, the water wave statistics indicate a reduction in wave height, which can be attributed to micro-breaking and nonlinear interactions among the waves. The ratio between the local depth in reference to the zero velocity surface (see Fig. 5) and the wavelength (see Longo, 2012, Table 3) is around 0.42 in all Sections and even smaller in Section 6, where it is only around 0.2. Hence the waves are not exactly in deep water, affecting all Sections except Section 6. The jump in the friction factor can be due to several factors, including this transition from shallow water to deep water waves.

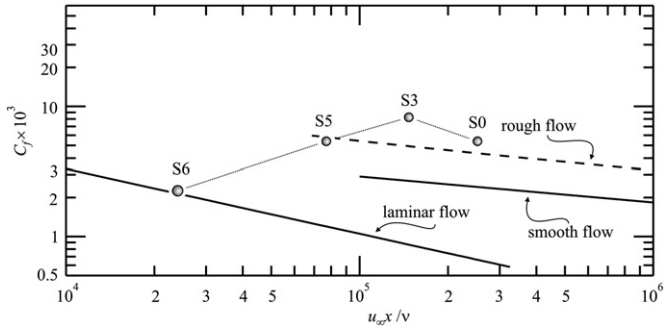

Fig. 7. The friction coefficient C_f as a function of the Reynolds number. Laminar, smooth turbulent and rough turbulent flows according to Eq. (11). ◎ represents data from these experiments in the 4 sections of measurements with identical wind speed. Test conditions in Tables 1 and 2.

3.3. Reynolds stresses

The profiles of the turbulent kinetic energy (TKE) and the Reynolds shear stress are shown in Fig. 8, and a close-up of the Reynolds tensor components for a single section is shown in Fig. 9. The horizontal component is dominant except at depths near $z = -H_{\mathrm{rms}}$. The angle of the principal axis is generally less than 35°, and a layer of constant shear stress can be observed close to the interface with $-\overline{\tilde{u}\tilde{v}} \approx 4u_{*w}^2$ where

$$\hat{u} = u' + \tilde{u}. \tag{13}$$

In general the Reynolds tensor can be interpreted as a combination of a wave-induced tensor and a tensor where the residual fluctuations are involved. A simple way to separate the two components is filtering with a cut-off frequency obtained by the analysis of the free-surface statistics spectrum. The technique has been applied to the experimental data obtained in Section S0 and the results are shown in Fig. 10. The symbol ~ indicates the wave-induced components, which are dominant near the free surface, as expected, but not immediately below the free surface. Even after subtracting the (estimated) wave induced components, Fig. 10 indicates almost uniform Reynolds shear stress of $-\overline{u'v'} \approx 2u_{*w}^2$. Assuming that the Reynolds shear stress acts at the top of the viscous sub-layer, the Reynolds shear stress can be estimated to be $-\overline{u'v'} \approx u_{*w}^2$, with the friction velocity evaluated by the local turbulence measurements. However, this assumption is not applicable here, because turbulence is also generated by micro-breaking close to the air–water interface. This turbulence source increases the local level of turbulence without affecting the velocity profile in the deeper region. The current experiment shows that its contribution to the Reynolds shear stress is in the scale of u_{*w}^2. This

Table 3
The free-surface statistics in the tests in which the UVP is used for the velocity measurements. H_{rms}, $a_{c\text{-}rms}$, $a_{t\text{-}rms}$ are the root mean square values of the wave height, of the crest and of the troughs, H_{ave} is the mean wave, $H_{1/3}$ is the one-third wave height.

	U_∞ (m/s)	H_{rms} (mm)	H_{ave} (mm)	$H_{1/3}$ (mm)	T_{ave} (s)	$T_{1/3}$ (s)	$f_{1/3}$ (Hz)	$a_{c\text{-}rms}$ (mm)	$a_{t\text{-}rms}$ (mm)	L_0 (mm)	c_0 (m/s)
S1 $x=620$ mm	7.59	2.79	2.56	3.77	0.10	0.13	7.96	1.72	1.27	25	0.196
	8.24	3.60	3.25	5.01	0.11	0.15	6.76	2.26	1.54	34	0.231
	8.93	4.45	3.98	6.23	0.12	0.16	6.27	2.80	1.89	40	0.249
	9.61	5.60	5.05	7.74	0.14	0.17	5.88	3.62	2.22	45	0.265
	10.30	5.84	5.22	8.17	0.14	0.17	5.78	3.75	2.33	47	0.270
	10.95	6.21	5.52	8.71	0.14	0.17	5.76	4.00	2.52	47	0.271
	11.28	6.51	5.79	9.17	0.13	0.18	5.70	4.14	2.69	48	0.274
S0 $x=720$ mm	7.59	3.49	3.16	4.80	0.12	0.15	6.65	2.21	1.47	35	0.235
	8.24	4.25	3.78	5.95	0.12	0.16	6.07	2.69	1.78	42	0.257
	8.93	5.41	4.72	7.52	0.13	0.17	5.89	3.42	2.45	45	0.265
	9.61	5.48	4.88	7.64	0.13	0.17	5.78	3.45	2.36	47	0.270
	10.30	6.29	5.58	8.73	0.14	0.18	5.51	3.88	2.81	51	0.283
	10.95	5.62	5.06	7.88	0.12	0.17	6.06	3.58	2.44	43	0.258
	11.28	6.50	5.76	9.27	0.14	0.19	5.27	4.03	2.79	56	0.296
S − 1 x = 820 mm	7.59	3.32	2.98	4.67	0.12	0.15	6.54	2.12	1.44	37	0.239
	8.24	4.55	4.07	6.39	0.13	0.17	5.84	2.91	1.90	46	0.267
	8.93	5.31	4.68	7.46	0.14	0.18	5.58	3.34	2.33	50	0.280
	9.61	5.03	4.48	7.09	0.13	0.17	5.81	3.16	2.14	46	0.269
	10.30	5.81	5.17	8.14	0.14	0.19	5.32	3.59	2.53	55	0.293
	10.95	6.07	5.38	8.59	0.15	0.19	5.13	3.74	2.68	59	0.304
	11.28	6.90	6.10	9.81	0.15	0.21	4.72	4.23	3.04	70	0.331

is consistent with the findings of Siddiqui and Loewen (2007), who concluded that micro-breaking was responsible for 40–50% of the near-surface turbulence.

In literature, there are several measurements in the field where the dissipation rate along the vertical direction is quantified (e.g. Jones and Monismith, 2008; Kudryavtsev et al., 2008; Young and Babanin, 2006). In absence of a detailed measurement of the three velocity components and their spatial gradient, with a high frequency and spatial resolution, all the evaluations are based on some assumptions, such as the existence of an inertial subrange in the spectrum of turbulence that implies the classical Kolgomorov −5/3 decay law. However, the emergence of the inertial subrange requires a Reynolds number based on the macroscale, namely $Re_\Lambda = u\Lambda/\nu$, larger than 10^5 (or at least larger than 4×10^3 with some weaker hypothesis, see Tennekes and Lumley, 1972). Such a high Reynolds number often cannot be achieved in laboratory experiments, although it is frequently observed in geophysical flows. In our experiments, the value of Re_Λ is always less than 10^3 (see Fig. 19), so no inertial subrange is expected. Hence, the dissipation rate analysis has no substantial basis, and therefore is not implemented.

3.4. Measurements with the UVP

The measurements with the UVP were limited to three sections: S1, S0 and S − 1. The measurements are conducted with different free-stream wind velocities from 7.59 m/s to 11.28 m/s (see Table 3). The free-stream wind velocity is measured at 70 mm above the still-water level using LDV. The measured velocity profile confirmed that the velocity at this point is almost uniform for all of the tests.

3.4.1. The water-level statistics and scales estimation

Table 3 was made according to the zero-up-crossing analysis, which shows a general increase in the wave heights with wind speed and a strong asymmetry of the waves, whose crests are more than 50% higher than troughs. Hence attention should be paid if the Stokes drift needs to be computed, because the correct expression for non-linear waves should be used. The dominant wavelength was computed based on the linear dispersion relationship. These are only reference values, since the effects of the current exist. Longo (2012) gives a detailed experimental evaluation of the wave celerity and of the wavelength.

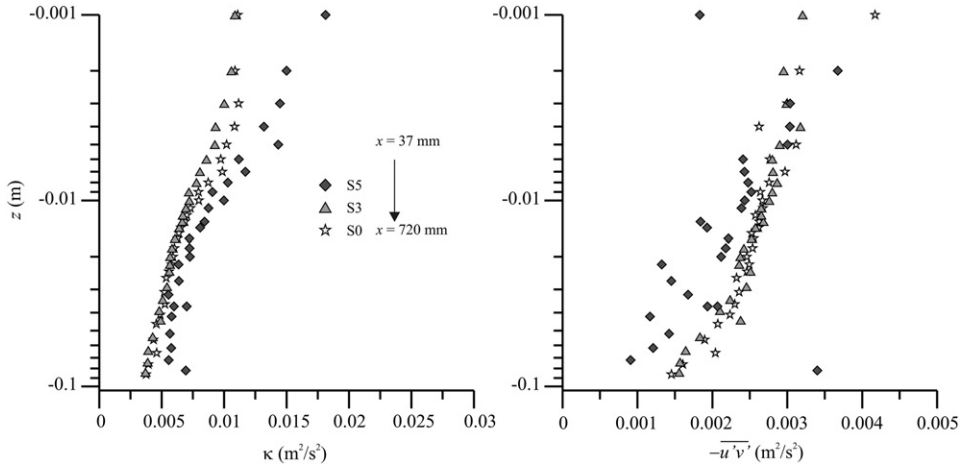

Fig. 8. The time-averaged turbulent kinetic energy and Reynolds shear stress from the LDV measurements in water.

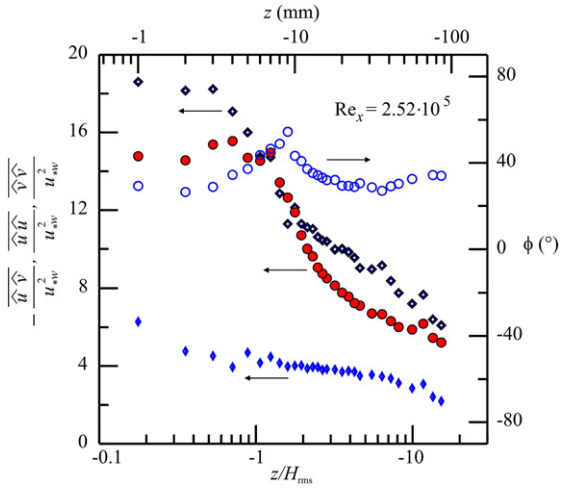

Fig. 9. The LDV measurements in water. The distribution of the time-averaged Reynolds stresses in Section S0 ($x=720$ mm). $u_{*w}=0.026$ m/s. $\nu=10^{-6}$ m^2/s. ◇, $\overline{\tilde{u}\tilde{u}}$; ●, $\overline{\tilde{v}\tilde{v}}$; ◊, $\overline{\tilde{u}'\tilde{u}'}$; ○, $-\overline{\tilde{u}'\tilde{v}'}$; ○ angle of the principal axis.

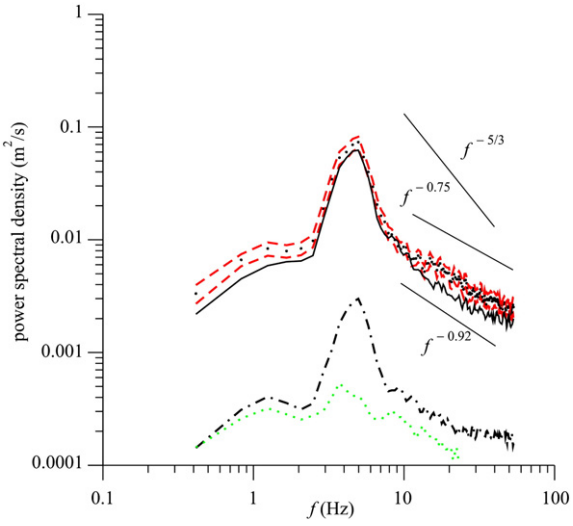

Fig. 11. The vertical velocity spectrum as measured by UVP in different gates. Dots and dashed line: Lagrangian reference system with the origin at the instantaneous water level, depth equal to 30 mm, with confidence band 95%; continuous line: Eulerian reference spectrum at $z=-40$ mm; dashdot line: Lagrangian reference system with the origin at the instantaneous water level, measurements at the free surface level (depth equal to 0); dotted line: Lagrangian reference system with the origin at the instantaneous water level, depth equal to 52.5 mm. Test $U_\infty=11.28$ m/s. Section S−1.

The spectrum of the velocities in a Lagrangian frame having origin at the instantaneous level and at three different depth is shown in Fig. 11. Also, a spectrum in an Eulerian frame at $z=-40$ mm is shown. For the spectrum in the Lagrangian frame, the peaks correspond to the dominant wave frequency, and the wave energy decays as $\approx f^{-0.75}$ in the range 10–40 Hz with a coefficient of determination $R^2=0.96$. For that in the Eulerian frame, it decays as $\approx f^{-0.92}$. A secondary peak is evident at around 1.5 Hz, which corresponds to a fundamental oscillation mode of the wave tank. The free-surface spectrum shows that most of the energy is stored in waves with frequencies from ~7 to ~5 Hz. Larger wind speed tends to generate lower frequency waves. The wave growth is also linked to an energy transfer from high frequency towards low frequency waves, owing to the nonlinear wave-wave interactions. This process is not monotonic, because part of the energy is dissipated with a reduction of the H_{rms} once wave breaking occurs. These spectra can be compared to a similar one in Jones and Monismith (2008), based on which they computed the energy dissipation. Their spectrum shows an inertial subrange with a −5/3 rate decay, whereas the decay is much slower in the present tests. Part of the differences can be attributed to the different reference system in velocity measurements, since a faster decay is achieved in the Eulerian frame (see continuous line in Fig. 11). The main reason that no inertial subrange (Kolgomorov interval) is achieved in the present tests is due to the limited Reynolds number Re_Λ, being always smaller than 10^3. A similar result can also be found in Young and Babanin (2006), although their data refer to waves with a frequency much lower than the present experiments waves.

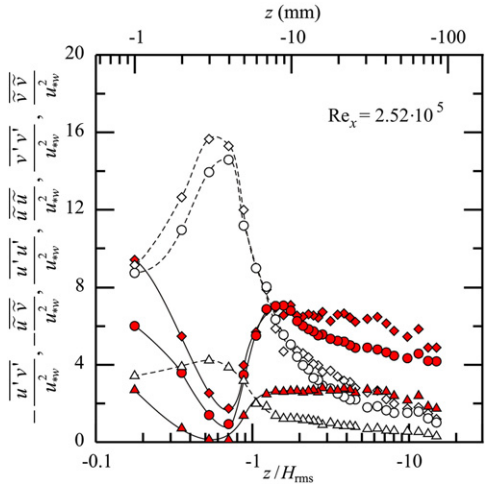

Fig. 10. The LDV measurements in water. The distribution of the mean turbulent and oscillating Reynolds stresses in Section S0 ($x=720$ mm). $u_{*w}=0.026$ m/s. $\nu=10^{-6}$ m^2/s. ◆, $\overline{\tilde{u}'\tilde{u}'}$; ●, $\overline{\tilde{v}'\tilde{v}'}$; ▲, $-\overline{\tilde{u}'\tilde{v}'}$; ◊, $\overline{\tilde{u}\tilde{u}}$; ○, $\overline{\tilde{v}\tilde{v}}$; Δ, $-\overline{\tilde{u}\tilde{v}}$.

Experiments on the free surface turbulence (Longo, 2010) have shown that, in the free-surface boundary layer, a proper length scale is H_{rms} and a proper velocity scale is $u_s=\sqrt{\overline{(dz_s/dt)^2}}$, where u_s is the root mean square of the free-surface vertical velocity and z_s is the instantaneous vertical position of the free surface. The material derivative can be approximated by a partial derivative, i.e., $dz_s/dt\approx\partial z_s/\partial t$. Other scales, such as the wavelength and the drift velocity, are supposed to act mainly in the horizontal direction, yet the focus here is in the vertical direction. Using the two aforementioned scales, we can define the following non-dimensional groups:

$$Fr_s=\frac{u_s}{\sqrt{gH_{rms}}},\ Re_s=\frac{u_sH_{rms}}{\nu},\ We_s=\frac{\rho u_s^2H_{rms}}{\sigma}. \tag{14}$$

The suffix s indicates that the parameters are associated with the free surface. The Froude number accounts for the proportion of the kinetic and gravitational energies in the free-surface fluctuations. The Reynolds number characterises the level of turbulence in the free-surface boundary layer, and the Weber number accounts for the relative importance of the surface tension, where σ is the surface tension coefficient. The three parameters for the present tests are reported in Table 4.

3.4.2. The mean vertical velocity and turbulence

The mean vertical velocity in Section S−1 is shown in Fig. 12. The velocity has negative values that compare favourably with the measurements obtained by LDV (see Fig. 4 for comparison). Phasic and mean Eulerian values are related by water concentration, i.e. the mean Eulerian velocity is equal to the phasic velocity multiplied by the water concentration, while the mean Lagrangian velocity profile, taken in a reference moving with the free-surface, shows a periodic modulation of ~2.5 H_{rms} around the still water level.

Table 4
The length and velocity scales and the Reynolds, Froude and Weber numbers computed for the present tests.

Section #	U_∞ (m/s)	H_{rms} (mm)	u_s (m/s)	Re_s (.)	Fr_s (.)	We_s (.)
S1, $x=620$ mm	7.59	2.79	0.066	184	0.40	0.17
	8.24	3.6	0.075	271	0.40	0.28
	8.93	4.45	0.089	395	0.43	0.48
	9.61	5.6	0.103	579	0.44	0.82
	10.3	5.84	0.107	622	0.45	0.91
	10.95	6.21	0.114	705	0.46	1.10
	11.28	6.51	0.121	785	0.48	1.30
S0, $x=720$ mm	7.59	3.49	0.071	247	0.38	0.24
	8.24	4.25	0.081	346	0.40	0.39
	8.93	5.41	0.118	637	0.51	1.03
	9.61	5.48	0.102	561	0.44	0.79
	10.3	6.29	0.12	756	0.48	1.25
	10.95	5.62	0.115	646	0.49	1.02
	11.28	6.5	0.116	755	0.46	1.21
S−1, $x=820$ mm	7.59	3.32	0.067	222	0.37	0.20
	8.24	4.55	0.083	376	0.39	0.43
	8.93	5.31	0.095	503	0.41	0.65
	9.61	5.03	0.09	454	0.41	0.56
	10.3	5.81	0.101	585	0.42	0.81
	10.95	6.07	0.104	631	0.43	0.90
	11.28	6.9	0.113	780	0.43	1.21

In the present analysis, the proper velocity scale is u_s. The non-dimensional profiles for all of the tests (increasing wind speed), including Section S0, are presented in Fig. 13. The phasic average shows large values near the wave crests, and large wind speeds induce the collapse of the profiles, especially in the wave crests. As for the mean velocity and turbulence, a spatial periodicity is evident. Similar results are obtained at the other two sections. At the mean water level, the vertical turbulence intensity can be expressed as $v'_{rms}/u_s = 0.33$, 0.35, 0.43 for Sections S1, S0 and S−1 (increasing fetch), i.e., turbulence becomes increasingly dominant. These values are close to the value of $v'_{rms}/u_s = 0.33$ as measured in a stationary flow generated by a Crump weir in a laboratory flume (Longo, 2011). Beneath the mean water level, the data are more dispersed. It is evident that the turbulence level peaks at $z = -H_{rms}$, especially with relatively small wind speeds (i.e., reduced H_{rms} and reduced microbreaking). Hence, if micro-breaking exceeds a threshold, then the turbulence level becomes less sensitive to the details of the flow characteristics and depends only on some integral properties, such as the wave height.

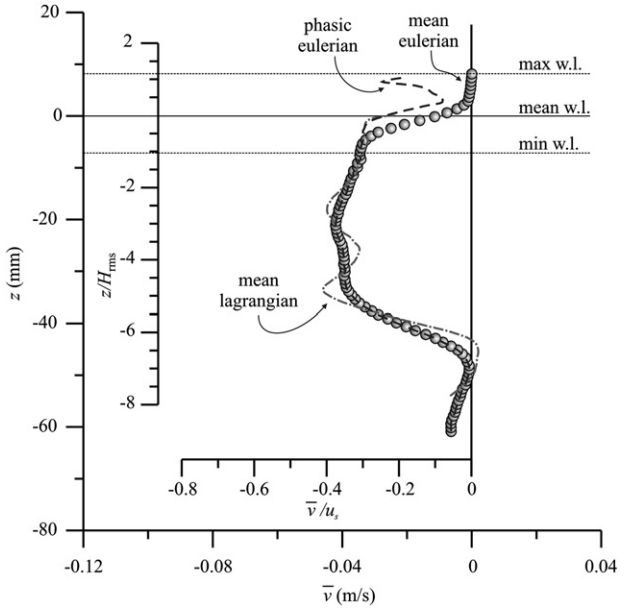

Fig. 12. The vertical mean Eulerian water velocity profiles. The phasic Eulerian average (dashed line) and the Lagrangian mean velocity (dash-dot line) is also shown. Test $U_\infty = 11.28$ m/s. Section S−1.

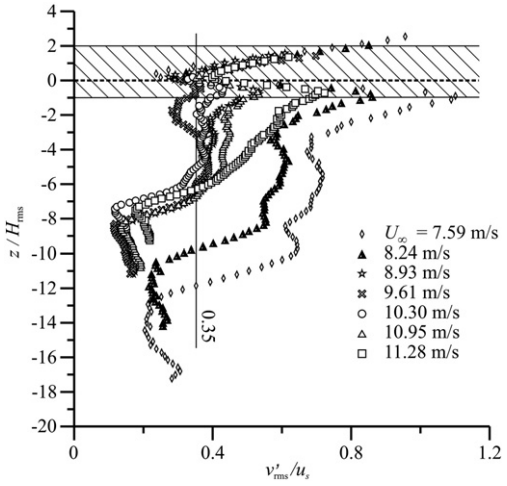

Fig. 13. The turbulence intensity, vertical component and phasic Eulerian average. Section S0. $x = 720$ mm.

For comparison, the LDV results in a test are shown in Fig. 14. LDV allows evaluation of the horizontal fluctuating component and thus the Reynolds shear stress. The vertical fluctuating component obtained by LDV is similar to that obtained by UVP near the free surface, and thus the overall behaviour of the flow is reproduced. Some discrepancies beneath $z/H_{rms} = -6$ can be attributed to the differences in the spatial resolution and temporal resolution of the two instruments.

4. Spatial structure of turbulence

The structure of the turbulence can be analysed by examining the two-point correlation at different depths below the surface. The two-point correlations are not homogeneous in a non-isotropic velocity field, so they have to be computed using the standard expression

$$R_{u_i u_j}(\mathbf{x}_1, \mathbf{x}_2) = E\left\{u_i'(\mathbf{x}_1) u_j'(\mathbf{x}_2)\right\}, \tag{15}$$

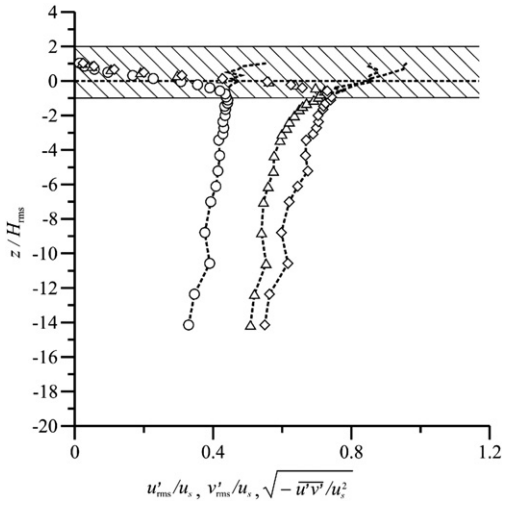

Fig. 14. The non-dimensional Reynolds stress values from the LDV measurements. The symbols are the time-averaged Eulerian values. The dashed line is the phasic Eulerian average. ◊: u'_{rms}/u_s; Δ: v'_{rms}/u_s; ○: $\sqrt{-\overline{u'v'}/u_s^2}$. $U_\infty = 11.28$ m/s. Section S0. $x = 720$ mm.

where E represents the ensemble average and the summation notation is not implied for i and j. The heterogeneity naturally arises from the presence of the flow boundaries. Due to the time lag between the velocity measurements at different positions, a correction is necessary for a proper evaluation of R_{u_iuj}. To achieve this, an algorithm is developed on the basis of a Taylor's series, neglecting the higher-order contributions, as reported in Longo (2011). Because we have only the vertical velocity components in the UVP measurement, only the properties of $R_{v'v'}$ in the vertical direction are described. Using the data, we can evaluate the function $R_{v'v'}(z_1,z_2) = E\{v'(z_1)v'(z_2)\}$ in a non-dimensional form

$$\chi_{v'v'}(z_1,z_2) = \frac{R_{v'v'}(z_1,z_2)}{\sqrt{R_{v'v'}(z_1,z_1)}\sqrt{R_{v'v'}(z_2,z_2)}} \equiv \frac{R_{v'v'}(z_1,z_2)}{v'_{\mathrm{rms}}(z_1)v'_{\mathrm{rms}}(z_2)}, \tag{16}$$

which can also be expressed as

$$\chi_{v'v'}(z,\zeta) = \frac{R_{v'v'}(z,\zeta)}{v'_{\mathrm{rms}}(z)v'_{\mathrm{rms}}(z+\zeta)} \tag{17}$$

where ζ is the space lag. The computed two-point correlations of the vertical fluctuating velocities along the vertical direction at one point are shown in Fig. 15.

The shape of the correlation function reveals the anisotropy of the turbulence and the presence of a wide spectrum of eddies. Nevertheless, some specific eddy contributions can be distinguished.

The expression for the autocorrelation of a simple eddy in the origin is (Townsend, 1976):

$$R_{v'v'} = \frac{1}{2}A\alpha^2\left(1-\frac{1}{2}\alpha^2\zeta^2\right)\exp\left(-\frac{1}{4}\alpha^2\zeta^2\right). \tag{18}$$

where A is a coefficient specifying the intensity of the eddy, having dimension $[L^4T^{-2}]$, α is a measure of the size of the eddy having dimension $[L^{-1}]$. The parameter α can be converted in terms of the radius $r_{1/e}$, – the distance between the eddy centre and the location where the vorticity is reduced by $1/e \approx 37\%$ times. Assuming that the correlation is between a series of simple eddies, the expression becomes

$$R_{v'v'} = \sum_i \frac{1}{2}A\alpha_i^2\left[1-\frac{1}{2}\alpha_i^2(\zeta-b_i)^2\right]\exp\left[-\frac{1}{4}\alpha_i^2(\zeta-b_i)^2\right]. \tag{19}$$

where b_i is the shift the i-th eddy from the orgin. A non linear least square fitting algorithm has been used to evaluate the coefficients A_i and α_i. A fitting curve according to this expression, with a coefficient of determination $R^2 = 0.94$ and with only three eddies included, is shown in Fig. 15. The three vortices have their centres $z = +1.2$, -31.6, -44.2 mm, size parameters $\alpha = 0.042$, 0.155, $0.063\ \mathrm{mm}^{-1}$ and intensities $A/\overline{v'^2} = 721.1,\ 21.1,\ 218.0\ \mathrm{mm}^2$ respectively. A better interpretation of the symbols is obtained by considering that $1/2A_i\alpha_i^2$ is proportional to the energy per unit volume (and mass density) associated with the i-th eddy. The fitted eddies have values $\left(1/2A_i\alpha_i^2\right)/\overline{v'^2} = 1.27,\ 0.51,\ 0.86$ and their radius is $r_{1/e} = 48.0,\ 12.9,\ 31.7$ mm respectively. While the most intense eddy is likely to be an artefact, being too close to the free surface, the other two eddies are more significant. The radii of these eddies are of the order of the length macroscale as defined and computed in the next Section (see Tennekes and Lumley, 1972, for a general description of the scales of the eddies). This means that the array of eddies in the studied flow field are extremely regular, as they can be detected so clearly, and allow a coherent description of the turbulent flow field. A typical contour map of the correlation function is shown in Fig. 16.

4.1. The macro- and microscales

Correlation functions can provide additional information about the structure of turbulence in terms of the macro- and micro-scales. Under the isotropic and homogeneous condition, the macroscale length Λ_{ij}, corresponding to the velocity component j in the direction x_i, is generally defined as

$$\Lambda_{ij} = \int_0^\infty \chi_{ij}(\Delta x_i)\, dx_i. \tag{20}$$

In heterogeneous and anisotropic flows, a better definition of the integral macroscale would be

$$\Lambda_{zj}(z) = \frac{1}{2}\int_{-\infty}^{\infty} \chi_{ij}(z,\zeta)\ \ d\zeta. \tag{21}$$

The integral macroscale is based on the autocorrelation of one of the three velocity components and is a function of the vertical position. For simplicity, we assume that the macroscales are representative of the three dimensions of the vortices in the following analysis, although this is not the case for strongly anisotropic

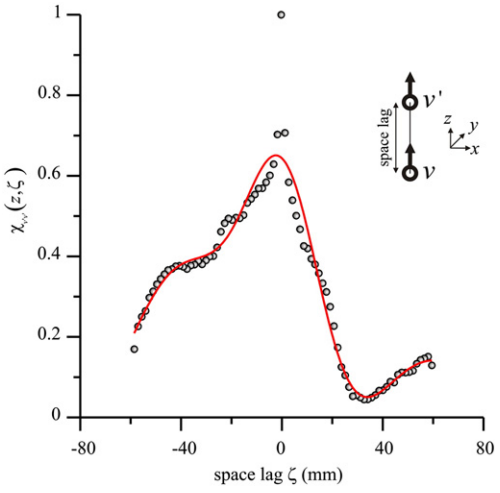

Fig. 15. The vertical two-point non-dimensional correlation. $\chi(z,\zeta)$at $z = -30$ mm. $U_\infty = 11.28$ m/s. Section -1. The bold line is a fitting function.

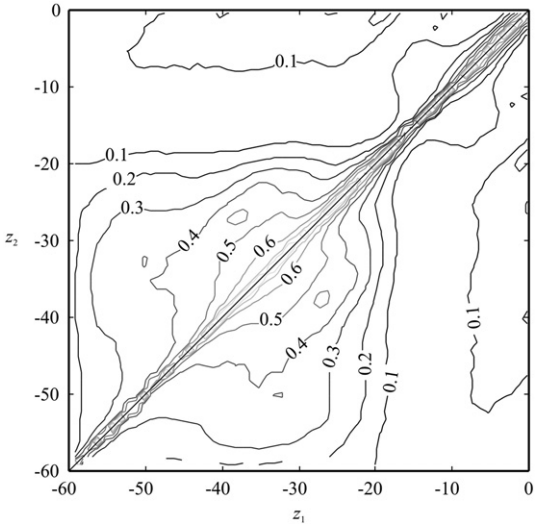

Fig. 16. A vertical two-point non-dimensional correlation. $\chi(z_1,z_2)$. $U_\infty = 11.28$ m/s. Section S – 1.

turbulence. If the correlation function does not decay sufficiently at the edge of the computational domain, an underestimation on the eddy size can be made. Often, the integral length scales are calculated by finding the intercepts of the power spectrum of the velocity fluctuations (Tennekes and Lumley, 1972). This study shows that the macro-scales of the turbulence, computed by integrating the correlation functions, are not sensitive to the passage of wave crests and troughs, and the dominant eddies seem to possess a constant pattern.

Amongst the numerous definitions of length microscales, a widely used one is the Taylor microscale, defined as

$$\lambda_{zz}(z) = -2\left|\frac{\partial^2 R_{v'v'}(z,\zeta)}{\partial \zeta^2}\right|_{\zeta=0} \equiv \frac{2\overline{v'^2}}{(\partial v'/\partial z)^2}. \tag{22}$$

This is not the smallest scale, but it is often assumed as the length scale for the majority of the dissipation to take place. The Taylor microscale was computed by performing the numerical evaluation of the spatial gradient in the denominator of the last expression in Eq. (22). As seen in Figs. 17 and 18, the length scales increase with water depth to maximum values, except in a layers close to the water surface, in which length scales first increase with depth up to $z \approx -H_{rms}$, then decrease with depth. The inset in Fig. 18 gives the variation of the Taylor microscale in the first layer beneath the free surface. In a large region beneath the thin surface layer, the maximum values of the length scales are limited by a straight line and are equal to $\Lambda_{max} \approx 0.4|z|$ and $\lambda_{max} \approx 0.06|z|$. Hence, the ratio of the two length scales is $\Lambda_{max}/\lambda_{max} \approx 6.7$.

A simplified turbulent energy budget can be revealed by the following equation (Tennekes and Lumley, 1972):

$$\underbrace{\bar{u}_j \frac{\partial}{\partial x_j}\left(\frac{1}{2}\overline{u'_i u'_i}\right)}_{I} = -\frac{\partial}{\partial x_j}\left(\underbrace{\frac{1}{\rho}\overline{u'_j p'}}_{II} + \underbrace{\frac{1}{2}\overline{u'_i u'_i u'_j}}_{III} - \underbrace{2\nu \overline{u'_i s'_{ij}}}_{IV}\right) - \underbrace{\left(\overline{u'_i u'_j}\right) s_{ij}}_{V} - \underbrace{2\nu \overline{s'_{ij} s'_{ij}}}_{VI}, \tag{23}$$

where s_{ij} is the rate of strain and the prime indicates the fluctuating component. If a local balance holds in isotropic turbulence, then the production (a term of scale u^3/Λ), expressed by the term *V*, equals the dissipation (a term of scale u^2/λ^2), which is expressed by the term *VI*. The energy dissipation in isotropic conditions, which is always satisfied at small scales and large Reynolds numbers, is equal to $15\nu\, u^2/\lambda^2$, while the production term is equal to $A\, u^3/\Lambda$, with the coefficient *A* being about unity. The balance requires:

$$\frac{\lambda_{zz}}{\Lambda_{zz}} = \sqrt{\frac{15}{A}}\,\mathrm{Re}_\Lambda^{-1/2}, \tag{24}$$

with the Reynolds number defined as $\mathrm{Re}_\Lambda = u\Lambda/\nu$. If the other terms in Eq. (23) are not negligible at small scales, as in the hypothesis of isotropy, the relationship between the two scales is

$$\frac{\lambda_{zz}}{\Lambda_{zz}} = a\mathrm{Re}_\Lambda^n, \tag{25}$$

where *a* is a coefficient. The gradient of pressure-work (term *II*) and the mean transport of turbulent energy by turbulent motion (term *III*) have the same scale as the production term, and thus cannot change the exponent of the relationship, i.e. $n = -1/2$, although they can modify the value of the coefficient. The transport by viscous stresses (term *IV*) is negligible at large Reynolds numbers, as it is of scale $u^3/(\Lambda \cdot \mathrm{Re}_\Lambda)$. The last possible contribution is the transport of turbulent energy by the mean motion (term *I*).

The length scale ratios for all of the tests in Section S−1 are shown in Fig. 19, and the results for all sections are listed in Table 5. The exponent is slightly less than −0.5, which is a typical value in local equilibrium. Hence, the Taylor microscale decreases faster than the macroscale. Assuming that the Taylor microscale is equal to the dissipative scale, the reduction of its value means a more efficient energy dissipation than the local equilibrium state. The faster energy decay rate is due to a net influx associated with the mean motion or the microbreaking at the free surface. A similar trend was also observed in the turbulence beneath a free surface generated by a Crump weir (Longo, 2011). If we assume that the exponent in Eq. (25) retains the value $n = -1/2$ and that the contributions of

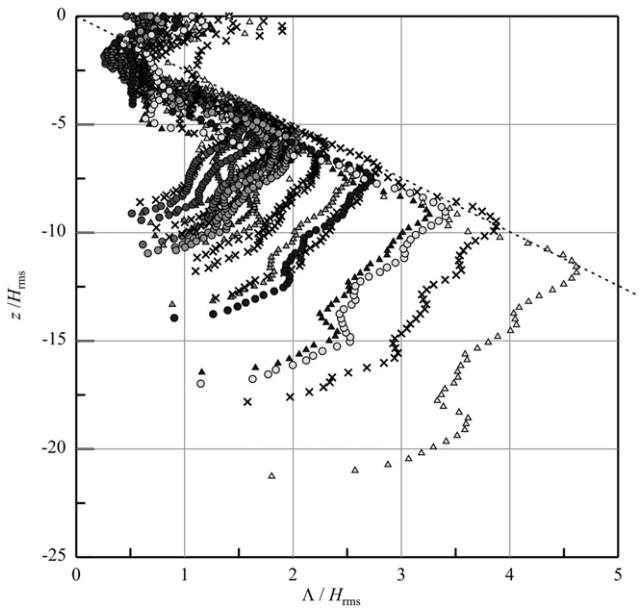

Fig. 17. The non-dimensional macroscale for all of the tests. The dashed line represents the equation $\Lambda_{max} = 0.4|z|$ for $|z| > 2.5\ H_{rms}$.

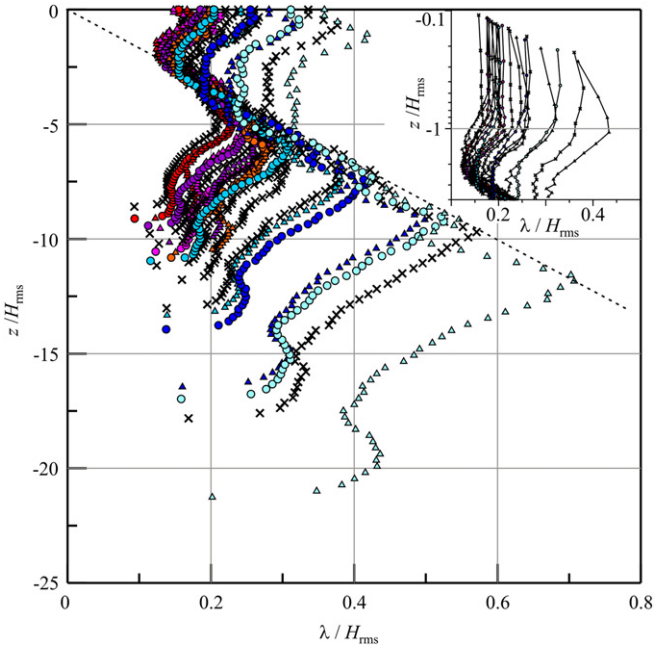

Fig. 18. The non-dimensional microscale for all of the tests. The dashed line represents the equation $\lambda_{max} = 0.06|z|$ for $|z| > 2.5\ H_{rms}$.

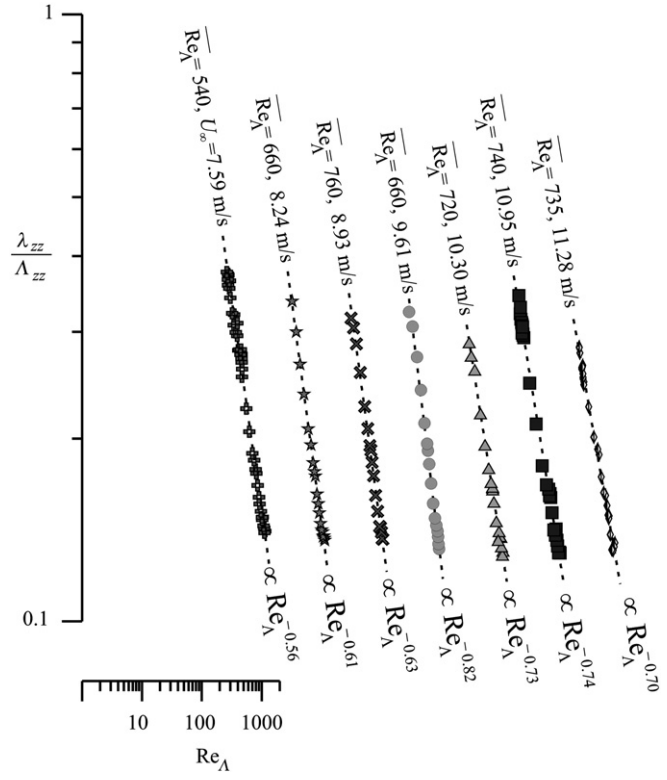

Fig. 19. The relationship between the microscale, macroscale and the Reynolds number. Section S − 1. $x = 820$ mm.

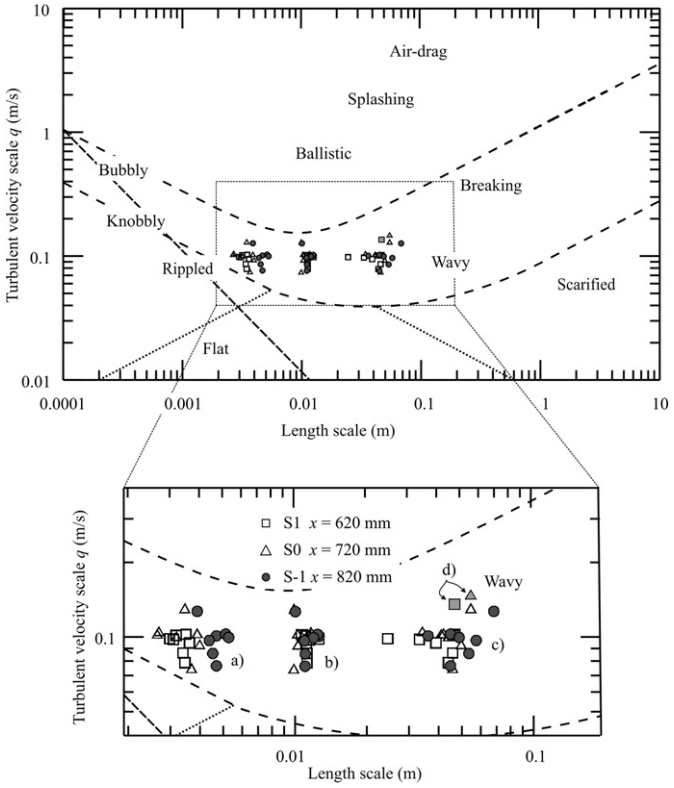

Fig. 20. A diagram of the turbulence velocity scale and length scale of the dominant surface features (Brocchini and Peregrine, 2001a,b). The symbols refer to the present experiments. a) The length scale is based on the integral scale (water side) near the free surface. b) The length scale is based on the maximum integral scale (water side). c) The length scale is equal to the gravity wavelength. d) The length scale is equal to the gravity waves wavelength, and the velocity scale is based on the combined turbulence level in the air side and in the water side.

the pressure-work and the mean transport of turbulent energy by turbulent motion are of the scale bu^3/Λ, then

$$\frac{\lambda_{zz}}{\Lambda_{zz}} = \sqrt{\frac{15}{A+b}}\,\mathrm{Re}_\Lambda^{-1/2}. \tag{26}$$

If A is of the order of 1, then the data reported in Table 5 show that the coefficient b is always negative and of the order 1. This result suggests that the net effect of the pressure-work and the mean transport of turbulent energy by turbulent motion is equivalent to a sink to turbulent energy. The pressure-work term is often neglected because the pressure tends to be poorly correlated with the velocity fluctuations except close to a wall or any other interface (Townsend, 1976).

Table 5
The coefficients and exponents of the relationship between the microscale, macroscale and the Reynolds number: $\lambda_{zz}/\Lambda_{zz} = a\mathrm{Re}_\Lambda^n$.

	U_∞ (m/s)	a	n
Section S − 1, $x = 820$ mm	7.59	5.54	−0.558
	8.24	8.42	−0.608
	8.93	10.59	−0.630
	9.61	35.26	−0.815
	10.30	21.85	−0.730
	10.95	23.59	−0.737
	11.28	18.96	−0.699
Section S0, $x = 720$ mm	7.59	6.49	−0.573
	8.24	8.15	−0.595
	8.93	13.20	−0.632
	9.61	37.26	−0.805
	10.30	28.53	−0.746
	10.95	24.20	−0.726
	11.28	20.49	−0.703
Section S1, $x = 620$ mm	7.59	3.82	−0.501
	8.24	7.31	−0.588
	8.93	11.93	−0.546
	9.61	29.55	−0.767
	10.30	18.75	−0.698
	10.95	17.42	−0.680
	11.28	21.81	−0.709

The classification of the flow regimes by Brocchini and Peregrine (2001a,b) is based on a velocity scale q, which is related to the TKE with $\kappa = \frac{1}{2}q^2$, and on a length scale L, which is related to the dominant surface features on the water side. In the present experiments, we estimated the wavelengths of the gravity waves and the vertical fluctuating velocity, from which the TKE can be easily extracted. Another length scale is the macroscale computed using the vertical correlation. The results are shown in Fig. 20a). The length scale is based on the integral scale of the water flow near the free surface, and the velocity scale is based on the TKE of the water flow. In Fig. 20b), the length scale is based on the maximum integral scale of water flow, and velocity scale is the same as in Fig. 20a). In Fig. 20c), length scale is equal to the gravity wavelength and the velocity scale is the same as in Fig. 20a) and b). In Fig. 20d), the length scale is equal to the wavelength of the gravity waves and the velocity scale is based on the combined turbulence level on both the air side and the water side. The combined velocity scale due to turbulence acting on both sides of the interface can be computed simply by assuming that the effective turbulence level is the weighted-average of the turbulence energy,

$$\frac{1}{2}q^2 = \frac{\rho_w\kappa_w + \rho_a\kappa_a}{\rho_w + \rho_a} \tag{27}$$

where ρ is the density and the subscript 'w' and 'a' stands for water and air, respectively.

4.2. The dissipation rate

The present laboratory experiments, with the measurements devices available to the authors, do not allow a direct evaluation of the dissipation rate, but useful hints can be obtained through field experiments. Young and Babanin (2006) show that the vertical profile of dissipation follows z^{-2}. A similar relationship is also reported in Jones and Monismith (2008), who proposed three relationships at different depths. A constant-dissipation layer happens in the range $-0.4\ H_s<z<0$, where H_s is the significant wave height; a power 2 decay layer (the exponent is -2.2) occurs in the range $-(d-zt3)<z<-0.4\ H_s$, where $zt3$ is the bed-stress log layer; and an increasing trend exists in the bed stress log layer $-d<z<-(d-zt3)$. Kudryavtsev et al. (2008) report similar results for the dissipation of turbulent energy. In addition, they show that the turbulent energy production at high wind speed is due to both wave breaking and shearing near the free surface (the role of wave breaking production decreases with the wind), but the wave breaking contribution becomes dominant in the water column up to the depth that the longest breaking waves penetrate. Similar findings are also reported in Huang and Qiao (2010).

In the present experiments, the expected distribution of the dissipation rate is not different from that depicted above. In addition, it is possibly influenced by the return current, which acts to limit the local water depth and generate a stable vortex, as revealed in the velocity correlation analysis. This vortex would add extra turbulent energy, inducing an intermediate layer with scales different from the free surface and to the bottom scales. Some indications on the dissipation rates can be inferred by the Taylor's microscale length profiles. Since smaller microscales mean larger energy dissipation, an increasing microscale length immediately beneath the free surface in the range $-H_{rms}<z<0$ (see inset in Fig. 18) supports the decreasing trend of the dissipation rate with depth.

5. Conclusion

- In our experiments, the mean turbulent velocity profiles are shown to be logarithmic, and the flows are hydraulically rough. The friction velocity for the water boundary layer is an order of magnitude smaller than that for the wind boundary layer. The level of turbulence is enhanced immediately beneath the interface due to micro-breaking, and this reflects that the Reynolds shear stress is of the order u_{*w}^2. It is consistent with numerous models in literature, which claims the existence of a layer immediately beneath the free surface where energy and momentum is added due to breaking waves (e.g. Kudryavtsev et al., 2008).
- The vertical components of the turbulent fluctuations take on common values of $v'_{\mathrm{rms}} = (0.32, 0.35, 0.43)\cdot u_s$ at the still-water level. The larger values correspond to larger fetches, similar to the case in a channel with a Crump weir.
- The autocorrelation function in the vertical direction shows features of typical anisotropic turbulence with a large range of wavelengths. The macro- and micro-scale increase with depths in a region below the free surface. Their maximum values take on $\Lambda_{\max} = 0.4|z|$ and $\lambda_{\max} = 0.06|z|$, respectively. Some permanent eddies are detected by analysing the autocorrelation functions.
- The ratio between the microscale and macroscale can be expressed as $\lambda/\Lambda = a\ \mathrm{Re}_\Lambda^n$, with the exponent n slightly different from $-1/2$, which is the value for the case with turbulence production and dissipation in balance. The negative value of the coefficient a indicates that the pressure-work and the mean transport of turbulent energy by turbulent motion act as sinks to turbulent energy.
- In the categorisation of the free-surface flows on the basis of a length scale and a turbulent velocity scale, the present experiments fall in wavy free-surface flow regime, if the wavelength is chosen as the length scale. The integral turbulent scale on the water side alone underestimates the degree of disturbance at the free surface, and correction can be made to include the air turbulence contribution. However, such a correction to the velocity scale is insignificant and does not significantly modify the classification of the flow regime at the interface in this study.

Acknowledgements

The experimental data presented herein were obtained during the first author's sabbatical leave at Centro Andaluz de Medio Ambiente (CEAMA), Grupo de Dinámica de Flujos Ambientales, University of Granada, Spain, kindly hosted by Miguel A. Losada. Financial support from CEAMA is gratefully acknowledged. Special thanks go Simona Bramato and Christian Mans, who provided help with the experiments.

References

Battjes, J.A., Sakai, T., 1981. Velocity field in a steady breaker. Journal of Fluid Mechanics 111, 421–437.
Brocchini, M., 2002. Free surface boundary conditions at a bubbly/weakly-splashing air–water interface. Physics of Fluids 14 (6), 1834–1840.
Brocchini, M., Peregrine, D.H., 2001a. The dynamics of strong turbulence at free surfaces. Part 1. Description. Journal of Fluid Mechanics 449, 225–254.
Brocchini, M., Peregrine, D.H., 2001b. The dynamics of strong turbulence at free surfaces. Part 2. Free-surface boundary conditions. Journal of Fluid Mechanics 449, 255–290.
Brumley, B.H., Jirka, G.H., 1983. Near-surface turbulence in a grid-stirred tank. Journal of Fluid Mechanics 183, 235–263.
Bye, J.A.T., 1965. Wind-driven circulation in unstratified lakes. Limnology and Oceanography 10, 451–458.
Cheung, T.K., Street, R.L., 1988. The turbulent layer in the water at an air–water interface. Journal of Fluid Mechanics 194, 133–151.
Chiapponi, L., Longo, S., Bramato, S., Mans, C., Losada, A.M., 2011. Free-surface turbulence, wind generated waves: laboratory data. Technical Report on Experimental Activity in Granada, University of Parma (Italy). CEAMA, Granada, Spain.
Churchill, J.H., Csanady, G.T., 1983. Near-surface measurements of quasi-Lagrangian velocities in open water. Journal of Physical Oceanography 13, 1669–1680.
Dankwerts, P.V., 1951. Significance of liquid-film coefficients in gas absorption. Industrial and Engineering Chemistry 43, 1460.
Dean, R.G., 1965. Stream function representation of nonlinear ocean waves. Journal of Geophysical Research 70 (18), 4561–4572.
Higbie, R., 1935. The rate of absorption of a pure gas into a still liquid during short periods of exposure. AIChE Transactions 31, 365.
Huang, C.J., Qiao, F., 2010. Wave-turbulence interaction and its induced mixing in the upper ocean. Journal of Geophysical Research, Oceans 115, C04026.
Jones, N.L., Monismith, S.G., 2008. The influence of whitecapping waves on the vertical structure of turbulence in a shallow estuarine embayment. Journal of Physical Oceanography 38 (7), 1563–1580.
Komori, S., Murakami, Y., Ueda, H., 1989. The relationship between surface-renewal and bursting motions in an open-channel flow. Journal of Fluid Mechanics 203, 102–123.
Komori, S., Nagaosa, R., Murakami, Y., 1993. Turbulence structure and mass transfer across a sheared air–water interface in wind-driven turbulence. Journal of Fluid Mechanics 249, 161–183.
Kudryavtsev, V., Shrira, V., Dulov, V., Malinovsky, V., 2008. On the vertical structure of wind-driven sea currents. Journal of Physical Oceanography 38, 2121–2144.
Lam, K., Banerjee, S., 1992. On the condition of streak formation in a bounded turbulent flow. Physics of Fluids A 4, 306–320.
Longo, S., 2010. Experiments on turbulence beneath a free surface in a stationary field generated by a Crump weir: free surface characteristics and the relevant scales. Experiments in Fluids 49, 1325–1338.
Longo, S., 2011. Experiments on turbulence beneath a free surface in a stationary field generated by a Crump weir: turbulence structure and correlation with the free surface. Experiments in Fluids 50, 201–215.
Longo, S., 2012. Wind-generated water waves in a wind tunnel: free surface statistics, wind friction and mean air flow properties. Coastal Engineering 61, 27–41.
McCready, M.A., Vassiliadou, E., Hanratty, T.J., 1986. Computer simulation of turbulent mass transfer at a mobile interface. AICHE Journal 32, 1108.
McKenna, S.P., 2000. Free-surface turbulence and air–water gas exchange. PhD Thesis, MIT.
Mori, N., Suzuki, T., Kakuno, S., 2007. Noise of Acoustic Doppler Velocimeter data in bubbly flows. Journal of Engineering Mechanics 133 (1), 122–125.
Nadaoka, K., 1986. A fundamental study on shoaling and velocity field structure of water waves in the nearshore zone. Technical Report No. 36. Dept. Civ. Engrg., Tokyo Inst. Tech.. 125 pp.
Rashidi, M., Banerjee, S., 1990. The effect of boundary conditions and shear rate on streak formation and breakdown in turbulent channel flows. Physics of Fluids A 2, 1827–1838.
Schlichting, H., Gersten, K., 2000. Boundary Layer Theory. Springer, Berlin.
Shemdin, O.H., 1972. Wind generated current and phase speed of wind waves. Journal of Physical Oceanography 2, 411–419.

Siddiqui, M.H.K., Loewen, M.R., 2007. Characteristics of the wind drift layer and micro-scale breaking waves. Journal of Fluid Mechanics 573, 417–456.
Sirkar, K.K., Hanratty, T.J., 1970. Turbulent mass transfer rates to a wall for large Schmidt numbers to the velocity field. Journal of Fluid Mechanics 44, 598.
Svendsen, I.A., 1984. Mass flux and undertow in a surf zone. Coastal Engineering 8, 347–365.
Tamburrino, A., Gulliver, J.S., 1999. Large flow structures in a turbulent open-channel flow. Journal of Hydraulic Research 37 (3), 363–380.
Tamburrino, A., Gulliver, J.S., 2002. Free-surface turbulence and mass transfer in a channel flow. AICHE Journal 48 (12), 2732–2743.
Tennekes, H., Lumley, J.L., 1972. A First Course in Turbulence. The MIT Press. ISBN: 0-262-20019-8, p. 300. + xii.
Thais, L., Magnaudet, J., 1996. Turbulent structure beneath surface gravity waves sheared by the wind. Journal of Fluid Mechanics 328, 313–344.
Thornton, E.B., 1979. Energetics of breaking waves in the surf zone. Journal of Geophysical Research 84, 4931–4938.
Townsend, A.A., 1976. The Structure of Turbulent Shear Flow. Cambridge University Press, Cambridge, UK.
Williams, J.M., 1981. Limiting gravity waves in water of finite depth. Philosophical Transactions of the Royal Society of London. Series A 302 (1466), 139–188.
Wu, J., 1975. Wind-induced drift current. Journal of Fluid Mechanics 68, 49–70.
Young, I.R., Babanin, A.V., 2006. Spectral distribution of energy dissipation of wind-generated waves due to dominant wave breaking. Journal of Physical Oceanography 36, 376–394.

List of the symbols

$<\ldots>$: space average operator
$\overline{\ldots}$: time average operator
$\tilde{\ldots}$: oscillating term operator
$\widehat{\ldots}$: phasic average operator
$\ldots'$: fluctuating plus oscillating contributions operator
$E\{\ldots\}$: ensemble average operator
β: tilting angle of the LDV probe
κ: turbulent kinetic energy
Φ_j: volume fraction or concentration for the j phase
Λ_{ij}: integral length scale in the i-direction on using the j-component fluctuating velocity
λ_{ij}: Taylor length scale in the i-direction on using the j-component fluctuating velocity
ρ, ρ_w: mass density, water mass density
σ: surface tension
ν: kinematic fluid viscosity
θ: LDV reference system rotation angle
χ: non dimensional two point correlation
τ: tangential stress
ζ: space lag
a: weighting function
a_c: crest height
a_t: trough height
C: constant
C_f: friction coefficient
c: celerity of propagation of Ultrasound, of the gravity waves
c_0: phase celerity of the gravity waves in absence of current
d: water depth
f_{co}: cut-off frequency
Fr, Fr_s: Froude number, based on free surface scales
FS: full scale
H, H_{rms}, H_{ave}: wave height, root mean square wave height, mean wave height
$H_{1/3}$, H_s: highest one-third wave, significant wave height
k: coefficient, von Karman constant
k_s: roughness length
L: length scale, wave length
PIV: particle image velocimetry
p: pressure
q: velocity scale
Q: volume discharge
$r_{1/e}$: radius correspondent to a decay equal to e^{-1}, e is the Neper number
$R_{u_i u_j}$: correlation function
Re, Re_x, Re_Λ, Re_s: Reynolds number, based on the abscissa x, based on the integral scale Λ, based on surface scales
s_{ij}: rate of strain
t: time
T_{ave}, $T_{1/3}$,…: period of the waves, mean value, mean value of the first third, …
TKE: turbulent kinetic energy
U: streamwise wind velocity
U_∞: asymptotic wind velocity
U_s: drift velocity
U_{sw}: wind induced drift velocity
U_{sS}: stokes drift velocity
UVP: ultrasonic Doppler velocity profiler
u, v: streamwise, vertical fluid velocity
u', v': streamwise, vertical fluctuating fluid velocity
u'_{rms}, v'_{rms}: streamwise, vertical root mean square value of the fluctuating fluid velocity
u_s: velocity scale
u_{*a}: friction velocity in the air boundary layer
u_{*w}: friction velocity in the water boundary layer
u_∞: asymptotic velocity of the water stream
We_s: Weber number, based on surface scales
x, y, z, x_i: spatial co-ordinates
$\mathbf{x}$, $\mathbf{s}$: space vector
X_j: phasic function for the j phase
z_s: instantaneous level of the free surface